

Weak lensing scattering transform: dark energy and neutrino mass sensitivity

Sihao Cheng (程思浩)^{1*} & Brice Ménard¹

¹*Department of Physics and Astronomy, The Johns Hopkins University, 3400 N Charles Street, Baltimore, MD 21218, USA*

26 July 2021

ABSTRACT

As weak lensing surveys become deeper, they reveal more non-Gaussian aspects of the convergence field which can only be extracted using statistics beyond the power spectrum. In Cheng et al. (2020), we showed that the scattering transform, a novel statistic borrowing mathematical concepts from convolutional neural networks, is a powerful tool for cosmological parameter estimation in the non-Gaussian regime. Here, we extend that analysis to explore its sensitivity to dark energy and neutrino mass parameters with weak lensing surveys. We first use image synthesis to show visually that, compared to the power spectrum and bispectrum, the scattering transform provides a better statistical vocabulary to characterize the perceptual properties of lensing mass maps. We then show that it is also better suited for parameter inference: (i) it provides higher sensitivity in the noiseless regime, and (ii) at the noise level of Rubin-like surveys, though the constraints are not significantly tighter than those of the bispectrum, the scattering coefficients have a more Gaussian sampling distribution, which is an important property for likelihood parametrization and accurate cosmological inference. We argue that the scattering coefficients are preferred statistics considering both constraining power and likelihood properties.

Key words: methods: statistical – gravitational lensing: weak – cosmological parameters – large-scale structure of Universe

1 INTRODUCTION

Statistical properties of matter density distribution in our Universe carry information about its components and evolutionary history. In the late-time universe probed by weak gravitational lensing distortion, or cosmic shear (see Bartelmann & Schneider 2001; Kilbinger 2015, for reviews), the non-linear growth of structure imprints non-Gaussianity at small scales. As a result, cosmological information starts to elude Gaussian statistics such as the power spectrum and correlation function (Rimes & Hamilton 2005, 2006; Neyrinck et al. 2006; Neyrinck & Szapudi 2007). To extract more information, some non-Gaussian statistics, such as the bispectrum (Fu et al. 2014), peak counts (Liu et al. 2015a,b; Kacprzak et al. 2016; Martinet et al. 2018; Shan et al. 2018), and Minkowski functionals (Petri et al. 2015), have been applied to existing weak lensing data. Deeper ongoing and future surveys like the Hyper Suprime-Cam survey (HSC, Aihara et al. 2018a,b), Rubin Observatory survey (formerly LSST, LSST Science Collaboration et al. 2009), *Euclid* (Laureijs et al. 2011), and Roman space telescope survey (formerly WFIRST, Spergel et al. 2015) have access to even smaller scales, making it increasingly important to employ proper statistics that can capture the non-Gaussian information in lensing maps (see, e.g., Martinet et al. 2021, and reference therein).

In Cheng et al. (2020), we proposed to use a non-Gaussian statistical tool that is novel to cosmology: the scattering transform¹.

We demonstrated its power by applying it to simulated weak lensing maps to constrain the Ω_m and σ_8 cosmological parameters. In this companion paper, we extend our analysis to other cosmological dependencies: the dark energy equation of state w_0 , w_a and the neutrino mass sum M_ν . Constraining these parameters is one of the key goals of upcoming weak lensing surveys and they are often used in the figure of merits to compare different survey strategies.

The scattering transform, introduced by (Mallat 2012) in the signal processing literature, uses concepts found in convolutional neural networks, but it needs no training: similar to traditional statistical estimators, it generates a set of summary statistics, which efficiently characterize complex non-Gaussianity at various scales. To visualize the power of scattering coefficients, we will first show that one can use them to generate random images with textures very similar to real lensing maps, to a level not achievable by traditional moment-based statistics such as the power spectrum and bispectrum. Then, we will present the constraining power of scattering coefficients for dark energy parameters and neutrino mass through a forecast using simulated lensing maps.

2 SCATTERING TRANSFORM

The scattering transform (Mallat 2012; Bruna & Mallat 2013) was originally developed in the context of signal processing in computer vision (see, e.g., Sifre & Mallat 2013; Andén & Mallat 2014; Bruna et al. 2015). In astrophysics, it has been used for parameter inference in cosmology (Cheng et al. 2020) and analysis of interstellar medium

* E-mail: s.cheng@jhu.edu

¹ To our best knowledge, the scattering transform has nothing to do with the scattering process in particle physics.

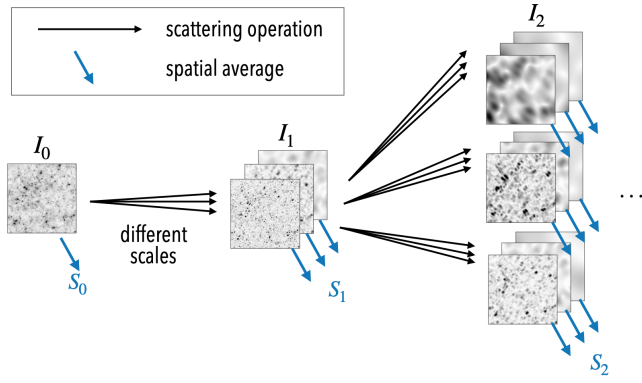


Figure 1. Structure of the scattering transform. From the input field, a tree of intermediate fields are generated by iterating the scattering operation, then the spatial averages of these fields, are taken as the translation-invariant scattering coefficients. The scattering operation is composed of a wavelet convolution and a pixelwise modulus.

(Allys et al. 2019; Saydjari et al. 2020; Regalado-Saint Blancard et al. 2020).

The scattering transform shares some properties with both convolutional neural networks (CNNs) and N -point correlation functions in desirable ways: it is powerful at extracting information from complex non-Gaussian fields, but it is deterministic, interpretable, and does not require any training. It compresses information into a relatively small set of coefficients due to its relation to wavelets, and it is a ‘first-order’ statistic, i.e. it does not use higher powers of the input field, which makes the scattering coefficients robust statistics.

On the one hand, the scattering transform can be understood as a CNN with pre-determined, non-trainable kernels. It inherits CNN’s way to extract spatial patterns, including local convolutions, a non-amplifying nonlinear operation, and multi-layers, but it abandons the learning ability which makes CNNs less controllable or interpretable.

On the other hand, as discussed in Cheng et al. (2020), the scattering transform is also similar to N -point functions averaged within wide, logarithmically-spaced bins, but with fundamental differences. Instead of using the multiplications of field intensities, the scattering transform uses a ‘low-order’ nonlinear operation to convert field fluctuations into their strengths. Therefore, the scattering transform does not amplify the tail of the underlying distribution function and thus alleviates the corresponding information loss problem (Carron 2011, 2012; Carron & Neyrinck 2012) of higher-order statistics. We will present a more in-depth comparison between the higher-order moments and scattering statistics in a forthcoming paper (Cheng & Ménard, in prep).

2.1 Formulation

The mathematics of scattering transform was introduced in Mallat (2012); Bruna & Mallat (2013). Here, we present a succinct introduction, following the notation in our first paper (Cheng et al. 2020). In brief, the scattering transform extracts information from a field by applying the following operations:

- wavelet convolution + modulus
- hierarchical structure
- spatial average

It can be formalized in a recursive way, as illustrated in Figure 1:

$$I_0 \equiv \text{input field} \quad (1)$$

$$I_n^{j,l} \equiv |I_{n-1} \star \psi^{j,l}| \quad (\text{the scattering operation}) \quad (2)$$

$$S_n \equiv \langle I_n \rangle, \quad (3)$$

where $\psi^{j,l}$ stands for a wavelet indexed by its scale j and orientation l .

The scattering operation is composed of a wavelet convolution followed by a pixelwise modulus. The function of convolution $\star \psi^{j,l}$ is to separate fluctuations into different scales; the function of modulus $|\cdot|$ is to convert the selected fluctuations into their local strengths. Successive applications of the scattering operation then form a tree structure, i.e. a planar multi-layer network, with various scattering fields I_n at its nodes. Each I_n is the intensity map of fluctuations of a particular scale in the previous-order field I_{n-1} . It can also be understood as a non-linear intensity map of a certain pattern in the input image I_0 .

Finally, the translation-invariant scattering coefficients S are defined as the spatial average of every scattering image, which resembles the pooling operation in convolutional neural networks. In this way, the 0th-, 1st-, and 2nd-order scattering coefficients can be written explicitly as:

$$S_0 \equiv \langle I_0 \rangle \quad (4)$$

$$S_1^{j_1, l_1} \equiv \langle I_1^{j_1, l_1} \rangle = \langle |I_0 \star \psi^{j_1, l_1}| \rangle \quad (5)$$

$$S_2^{j_1, l_1, j_2, l_2} \equiv \langle I_2^{j_1, l_1, j_2, l_2} \rangle = \langle |I_0 \star \psi^{j_1, l_1} \star \psi^{j_2, l_2}| \rangle. \quad (6)$$

The scattering operation which separates scales and measures fluctuation strength is qualitatively similar to the power spectrum analysis. Indeed, if we replace the modulus in Equation 2 by modulus squared, the scattering coefficients S_n will exactly become averaged 2^n -point functions weighted by a sequence of wavelets. However, the modulus instead of modulus squared makes it much more efficient in extracting information from the tail of the field probability distribution function (PDF).

The number of scattering coefficients S_n is determined by the number of distinct wavelets used. Using J scales and L orientations, the total number of coefficients up to the 2nd order is $1 + JL + J(J-1)L^2/2$. If orientation does not provide much relevant information, one may average over the directional indices:

$$s_n \equiv \langle S_n \rangle_{l_1, \dots, l_n}, \quad (7)$$

which reduces the number of coefficients to $1 + J + J(J-1)/2$, up to the 2nd order. For example, when using dyadic wavelets, a 512×512 pixel image has 8 wavelet scales ($J = 8$), corresponding to only 37 reduced scattering coefficients.

For more intuitive understanding of the scattering transform and coefficients, we refer the readers to Cheng et al. (2020); For more mathematical properties, we refer the readers to Mallat (2012) and Bruna et al. (2015).

2.2 Image generation based on scattering coefficients

To compare the performance of different statistics in characterizing a random field, it is informative to compare them through their image synthesis capabilities. Here we will focus on three statistics: the power spectrum, the bispectrum and the scattering coefficients in the context of weak lensing convergence maps. The idea of synthesis is to randomly generate new images (or, in other words, to sample from the ensemble of images) that have the same summary statistics as

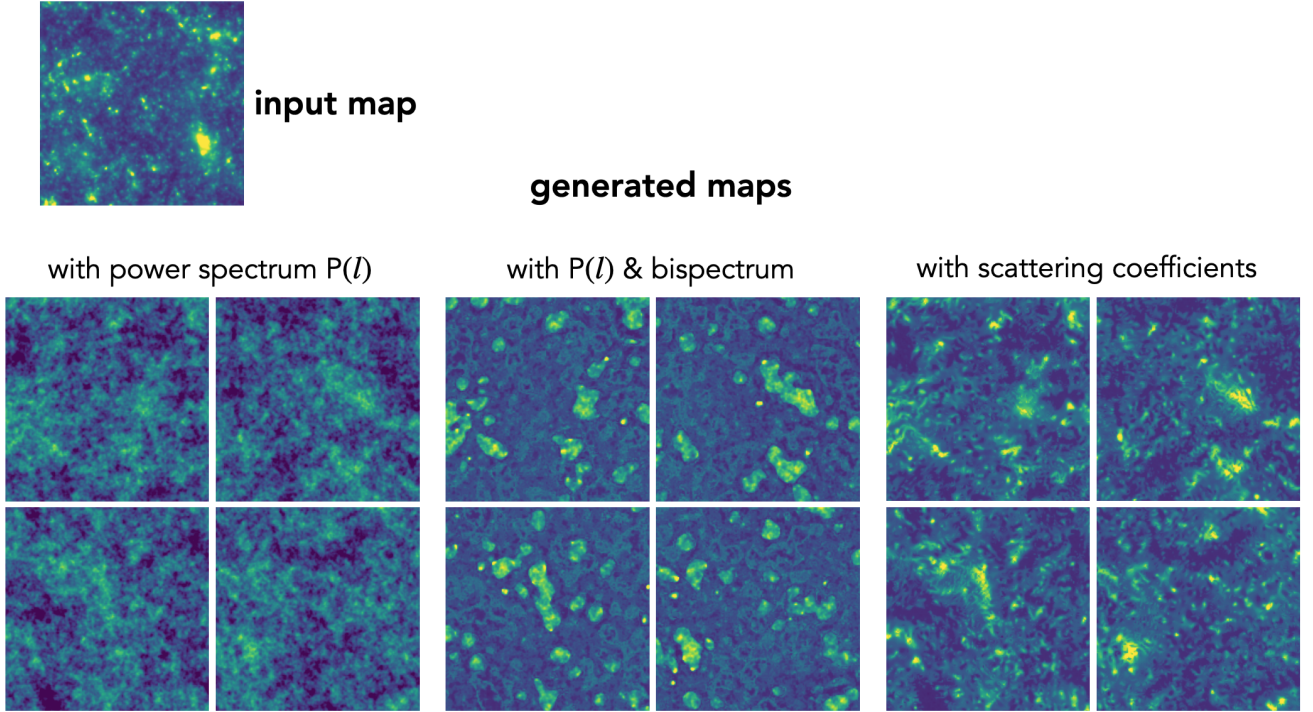


Figure 2. Images generated with selected sets of summary statistics, including the power spectrum, bispectrum, and scattering coefficients (S_1 , S_2), showing that the scattering coefficients characterize the field better. As the image generation is random, one should compare textures, instead of the exact positions of features, between the input and generated maps.

the target one, and then visually check the *texture* of the generated images (see, e.g., Bruna & Mallat 2019; Allys et al. 2020).

To implement it, we start from a random image and modify it in order to minimize the difference of the summary statistics between the generated and the target images. Technically, we start from a Gaussian random field that has the same power spectrum as the target image, and then use the ‘adam’ optimizer in the python package `torch.optim` to minimize a loss function defined from the difference of summary statistics between the generated and target image. In the scattering coefficient and bispectrum cases, we also minimize the difference of their L_1 norms and set a lower bound for all pixels. Our code for image generation is available online².

In Figure 2, we show the generated images using power spectrum P , bispectrum B , and the scattering coefficients S . For each set of statistics, four realizations are shown to illustrate the sampling variance. Compared to the power spectrum and bispectrum, the results from scattering coefficients look much more similar to a real lensing convergence map (target image), especially in the textures created by halos on all scales.

There are several caveats about image synthesis to keep in mind. For example, the image quality somewhat depends on the initial condition and the choice of loss function. More importantly, the concept of information must always be related to a particular task. In the image synthesis case, this task is ‘to distinguish fields under the metric of human eyes and brains’, which can be different from the Fisher information in the cosmological parameter inference task. Nevertheless, the striking visual similarity between the target and generated images using scattering coefficients is evidence of their power to characterize lensing map textures.

3 COSMOLOGICAL FORECAST

To explore the constraining power of the scattering coefficients on cosmological parameters, we calculate the Fisher forecast (Fisher 1935; Vogeley & Szalay 1996; Tegmark et al. 1997) and Bayesian posterior of the cosmological parameters, after building a likelihood emulator for the scattering coefficients using simulated lensing convergence maps.

3.1 Simulated lensing maps

To explore the effects of dark energy and neutrino mass on lensing scattering coefficients, we use two sets of simulated convergence maps, which were generously made available by the Columbia lensing team³. Both datasets were designed for probing the non-Gaussian information in weak lensing cosmology. The convergence maps were produced through ray-tracing N -body simulations to certain source redshifts without the Born approximation, using the `Lenstools` python package (Petri 2016). All the cosmologies are spatially flat. The first dataset, described in Petri (2016); Zorrilla Matilla et al. (2016); Liu et al. (2016), varies dark energy properties and matter density (w_0 , w_a , and Ω_m). The convergence is traced to one source redshift ($z = 2$). The second dataset, MassiveNuS (Liu et al. 2018), varies neutrino mass, matter density, and primordial fluctuation amplitude (M_ν , Ω_m , and A_s , equivalent to M_ν , Ω_m , and σ_8), and the convergence is traced to five source redshifts ($z = 0.5, 1, 1.5, 2, 2.5$). Both datasets contain multiple realizations of convergence maps in multiple cosmologies, with $3.5 \times 3.5 \text{ deg}^2$ field of view (where non-linear gravitational evolution becomes important) and 512×512 pixel

² https://github.com/SihaoCheng/scattering_transform

³ <http://columbialensing.org>

resolution. Thus these maps cover multipole moments l from 100 to roughly 30,000. Below we describe these datasets in more detail.

Dark Energy simulations: This dataset contains simulations of 7 w_0w_a CDM cosmologies with different dark energy properties, including the present dark energy density Ω_Λ and the dark energy equation of state index $w(a)$, parametrized by w_0 and w_a through $w(a) = w_0 + (1-a)w_a$ (Chevallier & Polarski 2001). Each simulation was run in a 240 Mpc/h box with 512^3 particles and used to generate 1,024 mock convergence maps with $3.5 \times 3.5 \text{ deg}^2$ field of view. The lensing sources were set at redshift $z = 2$. We down-sampled the original 2048^2 pixel maps to a 512^2 resolution with 0.41 arcmin per pixel, by averaging adjacent pixels. Besides the dark energy properties, other cosmological parameters are fixed: baryon density $\Omega_b = 0.046$, Hubble constant $h = 0.72$, scalar spectral index $n_s = 0.96$, normalization of fluctuation amplitude $\sigma_8 = 0.8$, effective number of relativistic degrees of freedom $n_{\text{eff}} = 3.04$, total neutrino masses $M_\nu = 0.0$, and temperature of the cosmic microwave background $T_{\text{CMB}} = 2.725 \text{ K}$. The dark matter density is set so that the universe is spatially flat, i.e., $\Omega_m = 1 - \Omega_\Lambda$. Pipelines for the N -body simulations and ray-tracing are described in Petri (2016), Zorrilla Matilla et al. (2016), and Liu et al. (2016). Specifications of the simulations are also listed on the website of the Columbia Lensing team.

Neutrino mass simulations (MassiveNuS): Generated by Liu et al. (2018), this dataset contains convergence maps for several source redshifts created from 101 $\Lambda\nu$ CDM simulations with different M_ν , Ω_m , and A_s (equivalent to M_ν , Ω_m , and σ_8). Other cosmological parameters are fixed: $\Omega_b = 0.046$, $h = 0.70$, $n_s = 0.97$, $w = -1$. Each simulation was run in a 512 Mpc/h box with 1024^3 particles and used to generate 10,000 convergence maps with $3.5 \times 3.5 \text{ deg}^2$ field of view and 512^2 -pixel resolution. The fiducial cosmology has parameters $(M_\nu, \Omega_m, A_s) = (0.1 \text{ eV}, 0.3, 2.1 \times 10^{-9})$. One cosmology with massless neutrinos $(M_\nu, \Omega_m, A_s) = (0 \text{ eV}, 0.3, 2.1 \times 10^{-9})$ is used to calculate the covariance matrix of summary statistics. In this study, we will use the convergence maps for 5 source redshifts ($z = 0.5, 1.0, 1.5, 2.0, \text{ and } 2.5$), in 28 cosmologies that are close to the fiducial cosmology, i.e. in the range of $A_s \in [1.8, 2.7] \times 10^{-9}$, $M_\nu \in [0.06, 0.60] \text{ eV}$, $\Omega_m \in [0.28, 0.32]$. This range of parameters is enough for estimating the scattering coefficients' constraining power for cosmological parameters in a Rubin-observatory-like survey.

In real lensing surveys, the galaxy shape noise will dilute cosmological information on small scales, acting as a scale cut. For simplicity, we approximate such noise by Gaussian white noise on convergence maps (van Waerbeke 2000), $\sigma_{\text{noise}}^2 = \langle \sigma_\epsilon^2 \rangle / n_{\text{gal}} A_{\text{pix}}$, where A_{pix} is the pixel area. We adopt an averaged ellipticity squared $\langle \sigma_\epsilon^2 \rangle = 0.3^2$ and a number density of background galaxies n_{gal} of 44 per arcmin² to simulate the weak lensing survey of the Rubin Observatory (LSST Science Collaboration et al. 2009). The multiple source redshifts of the MassiveNuS convergence maps also allow us to explore the information gain from redshift tomography. We consider two situations: (1) only the convergence maps for source redshift $z = 1$ are used, with $n_{\text{gal}} = 44$ per arcmin²; (2) convergence maps for five source redshifts are used, with $n_{\text{gal}} = 8.83, 13.25, 11.15, 7.36, \text{ and } 4.26$ per arcmin², respectively. The source densities are derived from the expected source redshift distribution for the Rubin Observatory survey: $n(z) \propto z^2 \exp(-2z)$ with a normalization of 50 per arcmin² (LSST Science Collaboration et al. 2009). We calculate the galaxy number density in each fiducial redshift bins by integrating the distribution from $z = 0.25$ to 2.75 with steps of $\Delta z = 0.5$ as the bin widths. For noisy maps, we also carry out a smoothing with Gaussian kernel $\sigma = 1$ arcmin. Finally, the effects of masks and imperfection in shear-to-convergence conversion (e.g., Kaiser &

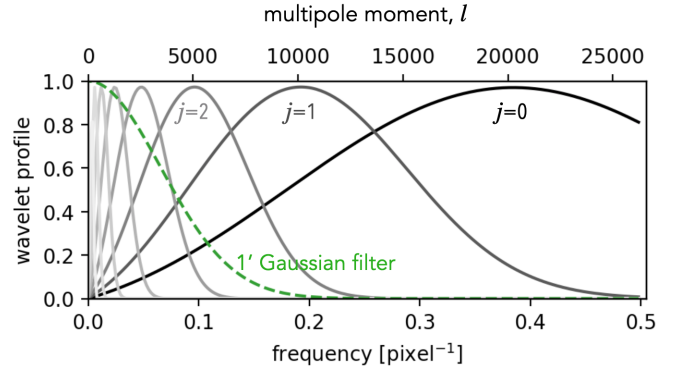


Figure 3. Scale coverage of wavelets used by the scattering transform. We also show the profile of a 1 arcmin Gaussian filter in frequency space for comparison.

Squires 1993; Pires et al. 2020; Jeffrey et al. 2020), which are important practical problems for weak lensing cosmology, are not taken into account in this analysis. Our primary goal is only to compare the statistical properties of different estimators.

3.2 Summary statistics

We calculate three sets of summary statistics from the simulated lensing convergence maps:

- 30 binned power spectrum $P(l)$ which we sample with linear bins of scale,
- 125 binned bispectrum $B(l_1, l_2, l_3)$ which are sampled within 10 linear bins for each of $l_1, l_2, \text{ and } l_3$ in the bispectrum monopole $B(l_1, l_2, l_3)$, and
- 36 reduced scattering coefficients s_1^j and $s_2^{j_1, j_2}$.

For the scattering coefficients, we use the same Morlet wavelets as described in Cheng et al. (2020), with 4 azimuthal orientations ($L = 4$) and 8 dyadic scales ($J = 8$). The scales correspond to 8 logarithmic bins from $l = 100$ to 37,000, as shown in Figure 3. Following Equation 7, we average over the azimuthal orientations and use the 36 reduced scattering coefficients s_1 and s_2 . On noisy maps, the small- j (small scale, high- l) scattering coefficients are dominated by noise, and we verify that abandoning the small- j coefficients does not change the precision of cosmological inference. As a result, the set of informative scattering coefficients on noisy maps is even more compact than on noiseless maps, which is desirable for inference analysis. As these scattering coefficients are non-negative, we instead consider their logarithm. This step helps to Gaussianize their PDF, which is a desired property for likelihood inference. We have also checked that this transformation has negligible effects on cosmological parameter inference. In the rest of the paper, we will always consider the logarithm of the coefficients but simply refer to them as scattering coefficients for brevity. We point out that the log-transform cannot be applied to the bispectrum coefficients which can be both positive and negative.

In summary, for each $3.5 \times 3.5 \text{ deg}^2$ lensing map, we calculate 36 scattering coefficients, 30 binned power spectrum coefficients, and 125 binned bispectrum coefficients for the cosmological parameter inference. We have developed a python3 package optimized in speed to calculate the translation-invariant scattering coefficients. The package, together with codes calculating the bispectrum, are available

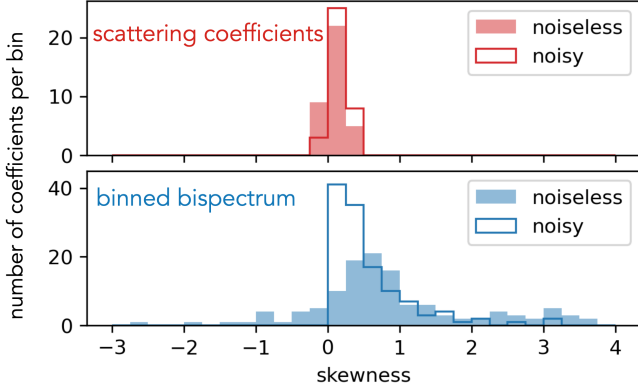


Figure 4. Skewness distribution of the (log) scattering and (binned) bispectrum coefficients, measured from 10,000 realizations of convergence maps at the fiducial cosmology of MassiveNuS simulation set. If the PDF of these statistical coefficients are Gaussian, then the skewness should be zero.

online⁴. We estimated the power spectrum using the `Lenstools` python package (Petri 2016).

3.3 Likelihood and parameter inference

Parameter inference requires a likelihood function $p(\mathbf{x}|\theta)$. We first assume that its function form is Gaussian, i.e., the probability distribution function (PDF) of the summary statistics \mathbf{x} is a multivariate Gaussian distribution for a given cosmology θ . We also assume the cosmological dependence of the mean vector of the Gaussian PDF can be approximated by a smooth function in the range of interest. For the dark energy dataset, we use a linear dependence, because there are only 7 cosmologies. For the MassiveNuS dataset, we use second-order polynomials. We set the covariance matrix to be independent of cosmology. The latter assumption is conservative but robust when the likelihood is not exactly Gaussian (Carron 2013). The cosmological dependence of mean vector and the covariance matrix are estimated using the simulated convergence maps.

Given the likelihood, we use the Fisher matrix and Bayesian posterior to quantify the constraining power of lensing scattering coefficients for cosmological parameters. The mathematical formulations of the inference frameworks are given in Appendix B. The Fisher matrix allows us to forecast the constraining power using only on the local cosmological dependence of the likelihood. For the noiseless cases we consider in this paper, it provides almost identical results as the posterior. However, with increasing noise level, the difference may become non-negligible. We will therefore use the Bayesian posterior for the results of noisy data.

4 RESULTS

4.1 The sampling distribution of summary statistics

Before exploring the constraining power on cosmological parameters, we first present one key advantage for using the scattering coefficients, namely that their probability density distribution (PDF) or sampling distribution is well Gaussianized.

For many cosmological studies, the typical inference framework

Table 1. Number of directions that are significantly non-Gaussian in the high-dimension PDF of summary statistics. Values outside and inside parentheses are for noiseless and noisy maps, respectively. Rows are different criteria to identify non-Gaussianity, which systematically suggest that the scattering coefficients have nearly-Gaussian PDF, whereas the bispectrum coefficients do not.

summary statistics number of coefficients	log scattering coefficients 36	binned bispectrum 125
$ \text{skewness} > 0.5$	0 (0)	87 (49)
$ \text{skewness} > 1$	0 (0)	45 (22)
$\text{kurtosis} > 0.5$	1 (1)	120 (78)
$\text{kurtosis} > 1$	0 (0)	111 (49)
whitened, $ \text{skewness} > 0.5$	0 (0)	18 (4)
whitened, $ \text{skewness} > 1$	0 (0)	9 (2)
whitened, $\text{kurtosis} > 0.5$	0 (0)	124 (25)
whitened, $\text{kurtosis} > 1$	0 (0)	119 (11)

assumes a Gaussian PDF for the statistical estimator. This is the so-called Gaussian likelihood assumption, though strictly speaking, likelihood is $p(\mathbf{x}|\theta)$ with the data \mathbf{x} fixed, while in practice one usually parametrizes and fits the PDF (the same expression with the model parameters θ fixed) to simulations. So we will call it the Gaussian PDF assumption. This assumption comes from the central limit theorem when the field of view tends to infinity. However, with a finite field of view, there is no guarantee for a Gaussian PDF (e.g., Sellentin & Heavens 2018; Hahn et al. 2019; Diaz Rivero & Dvorkin 2020; Jeffrey et al. 2021), and approximating a non-Gaussian PDF with a Gaussian one may introduce bias and/or underestimation of uncertainty to parameter inference. Therefore, summary statistics that Gaussianize quickly are favoured. Note that the non-Gaussianity of the field is not the same as the non-Gaussianity of the summary statistics. Some statistics of a highly non-Gaussian field can be nearly Gaussian distributed due to central limit theorem. On the other hand, statistics of a Gaussian random field can have non-Gaussian sampling distribution. For example, the power of each Fourier mode is expected to have a χ^2 -distribution.

Deviations from the Gaussian PDF approximation are harmful to inference, among which the most problematic is the presence of a heavy tail. To quantify this effect, we will consider both the skewness and kurtosis parameters of the 1D marginal distributions. More precisely: we calculate these parameters for both noiseless and noisy maps, using the fiducial cosmology of MassiveNuS simulation with source redshift $z = 1$. The skewness is defined as $\langle (\frac{x-\mu_x}{\sigma_x})^3 \rangle$ for each summary statistic x , where μ and σ are the sample mean and standard deviation calculated from the 10,000 realizations. It measures the asymmetry and tail heaviness of the one-variable PDFs, which is one possible deviation from a Gaussian distribution. The scattering coefficients⁵ have much lower skewness than the bispectrum coefficients. We show the histograms of their skewness parameters in Figure 4. Similarly, we measure the kurtosis defined as $\langle (\frac{x-\mu_x}{\sigma_x})^4 \rangle - 3$, which is more sensitive to the tail heaviness. For a 1D Gaussian distribution, given our sample size, the skewness and kurtosis should be 0 ± 0.03 and 0 ± 0.05 , respectively. The measured values for the scattering coefficients are indeed much closer to these expectations than the values obtained from the bispectrum which, in some cases, exceed the upper

⁵ We point out that, even without taking the logarithm of the scattering coefficients, the skewness values of the ‘raw’ scattering coefficients are still relatively small, typically between 0 and 1.

⁴ https://github.com/SihaoCheng/scattering_transform

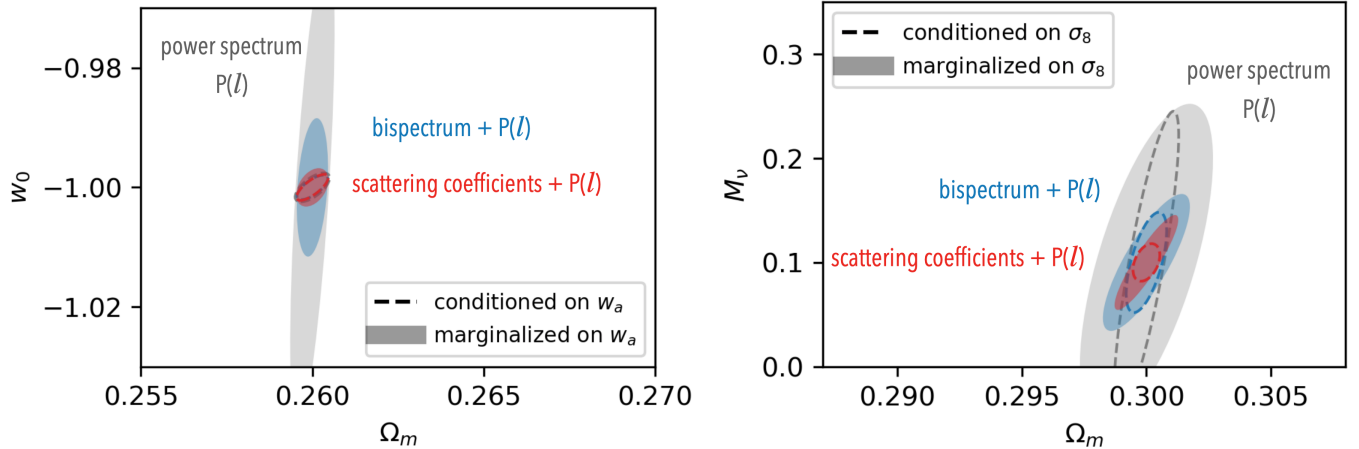


Figure 5. Fisher forecast with noiseless κ maps (95% confidence ellipses). The scattering coefficients have remarkably high constraining power for cosmological parameters. *Left:* Forecast for dark energy equation of state index $w(a) = w_0 + (1 - a)w_a$, from 20,000 deg^2 noiseless map with l nominally up to roughly 30,000 and source redshift $z = 2$. *Right:* Forecast for neutrino mass M_ν , from 20,000 deg^2 noiseless map with source redshift $z = 1$.

bound by more than two orders of magnitude. The effect of global whitening (using principle component analysis to remove correlations between dimensions) is also examined. Under all these metrics, the scattering coefficients show a low non-Gaussianity. In contrast, many dimensions of the bispectrum data vector are asymmetric or heavy tailed, even on the noisy maps where the field itself is more Gaussian. This is shown in Table 1 where we present the number of coefficients exceeding a given skewness or kurtosis threshold for each estimator. Tests using the 95-percentile, yet another measure of tail heaviness, show similar results. Assessing the non-Gaussianity of parameters in high-dimensional spaces can be done from numerous points of view. For example, Sellentin & Heavens (2018) proposed to use all pairs of 2D marginal PDFs. Such tests will be valuable in future studies aimed at inferring cosmological parameters.

The difference in the types of distributions found for scattering and bispectrum coefficients can be understood from their respective designs. The bispectrum coefficients are products of three random variables. The multiplication in general yields a distribution with heavier tail than the original variables. In contrast, the scattering transform uses a ‘first-order’ modulus which does not amplify the tail. Therefore, as the field of view increases, the central limit theorem Gaussianizes the scattering coefficients much quicker than bispectrum coefficients. Moreover, the logarithmic binning of scales through wavelets combines more Fourier modes, which also helps the Gaussianization process.

In summary, we find that the scattering coefficients Gaussianize particularly well, which is desirable and necessary for accurate cosmological inference.

4.2 Constraining cosmological parameters

Having checked the Gaussian PDF assumption for the scattering coefficients, now we compare the cosmological constraints obtained by different summary statistics. These constraints were obtained based on simulated convergence maps with varied cosmological parameters, and 1,000 (for the dark energy simulation set) or 10,000 (for the neutrino mass simulation set MassiveNuS) realizations for each cosmology.

Because the convergence maps have a long-tailed PDF (approximately log-normal), we do expect the scattering coefficients to extract more information than the bispectrum. Indeed, we find a significantly

tighter constraint using the scattering coefficients on noiseless maps (when all high- l modes are included). In Figure 5 we show the Fisher forecast of cosmological parameters using noiseless convergence maps, which corresponds to l from 100 to roughly 30,000. For simplicity, we only show a plane of two parameters for each dataset. In both panels of Figure 5, the marginalized ellipses are the projection of the three-parameter Fisher ellipsoids onto the plane, while the conditioned ellipses are their cross-sections.

For dark energy parameters (left panel), the power spectrum constrains w_0 well when w_a is known (conditioned), but constrains poorly if w_a is also to be constrained (marginalized), meaning a strong degeneracy between w_0 and w_a . Compared to the bispectrum, which is known to partly break this degeneracy (Takada & Jain 2003), the scattering coefficients almost eliminate it in the noiseless case. In weak lensing cosmology, there is another well-known degeneracy between Ω_m and σ_8 , which the scattering coefficients can also break (Cheng et al. 2020). However, the dark energy dataset used in this study has a fixed σ_8 value. So, it remains to be investigated whether or not the scattering coefficients can break both degeneracies at the same time.

On the noiseless maps, scattering coefficients also provide much tighter constraint on the neutrino mass sum M_ν than the power spectrum and bispectrum (see the right panel of Figure 5). In the parameter space spanned by Ω_m , σ_8 , M_ν , the power spectrum’s constraining power comes mainly from its overall amplitude, which results in a disc-like Fisher ellipsoid. Adding the bispectrum reduces the disc’s area by partly breaking the Ω_m – σ_8 degeneracy, whereas adding the scattering coefficients almost eliminate it, reducing it to a one-dimension instead of two-dimension degeneracy. This is consistent with the finding presented in the figure 5 of Cheng et al. (2020). The ratio between the volumes of the three-parameter Fisher ellipsoids (i.e., the square root of determinant of the covariance matrix) shown in the right panel of Figure 5 is roughly 20:4:1.

When the galaxy shape noise is taken into account, the constraining power of all summary statistics weakens due to the loss of small scale (high- l) information. In Figure 6 we show the forecast of neutrino mass sum (M_ν) for a Rubin-observatory-like survey, using the Bayesian posterior with fiducial cosmology at $(M_\nu, \Omega_m, A_s) = (0.1 \text{ eV}, 0.3, 2.1 \times 10^{-9})$. In spite of noises, there are still substantial non-Gaussian structures in the lensing convergence maps, thus the scattering coefficients still set much tighter cosmological constraints (more

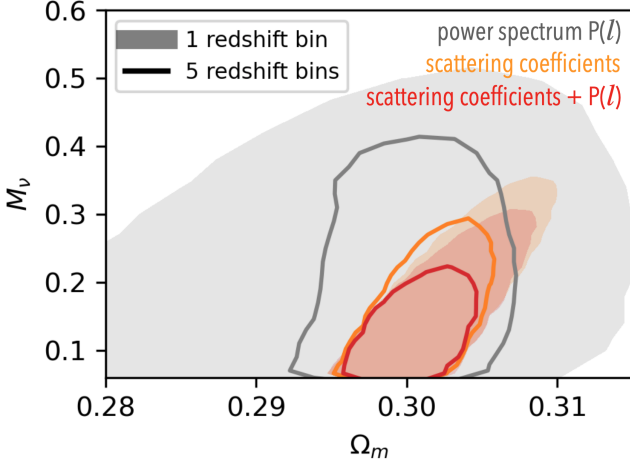


Figure 6. Forecast of cosmological parameters (95% confidence contours) for a Rubin-observatory-like survey with 20,000 deg² field of view, with M_ν , Ω_m , and A_s (or σ_8) to be constrained. Colours represent results of different sets of summary statistics of lensing convergence (κ). Improvement from adding redshift tomography is also shown.

than two times in M_ν) than using the power spectrum alone. In this noisy case, the combination of bispectrum and power spectrum sets a similar constraint to the combination of scattering coefficients and the power spectrum (though not shown in the figure). Figure 6 also show the effect of redshift tomography. A five-bin redshift tomography improves the scattering coefficients’ constraint for M_ν by about 40%.

With the same dataset (MassiveNuS), similar explorations were performed for other non-Gaussian statistics, including the PDF (Liu & Madhavacheril 2019; Boyle et al. 2021), bispectrum (Coulton et al. 2019), peak count (Li et al. 2019), starlet peak count (Ajani et al. 2020), minima count (Coulton et al. 2020), Minkowski functionals (Marques et al. 2019), and starlet l_1 -norm (Ajani et al. 2021). They all found similar improvement from redshift tomography for their respective summary statistics.

5 CONCLUSIONS

In cosmology, substantial information is stored in non-Gaussian structures on small scales, which requires statistics beyond the power spectrum to extract. Motivated by ongoing and upcoming deep surveys, we explore the weak lensing application of a novel and powerful non-Gaussian statistics, called the scattering transform. We extend the constraining forecast of Ω_m and σ_8 in Cheng et al. (2020) to more cosmological parameters including the dark energy parameters w_0 , w_a and neutrino mass M_ν . To do so, we use mock convergence maps from two publicly available simulation suites (the dark energy and MassiveNuS sets) made by the Columbia Lensing team.

We first show that using the scattering coefficients, one can generate random images with textures very close to a simulated lensing map, which cannot be achieved by using the power spectrum and bispectrum coefficients. Then, we show that the scattering coefficients provide significantly better constraint for dark energy parameters w_0 , w_a and neutrino mass M_ν than using power spectrum alone.

For noiseless maps (when high- l modes are accessible), the scattering transform also outperforms the bispectrum and power spectrum. This result can be explained by the ‘first-order’ nature of scattering coefficients which stay proportional to the field intensity, in contrast

to higher-order statistics which amplify the distribution tail. This lower-order nature together with the wavelet weighting strategy efficiently concentrates cosmological information into a compact set of scattering coefficients. Moreover, the lower-order nature makes the distribution of scattering coefficients much more Gaussian and robust than higher-order statistics, which is essential for accurate likelihood parametrization and parameter inference.

We also provide a forecast of M_ν with a noise level of the Rubin observatory survey, where the scattering coefficients set a 2 times tighter constraint than using the power spectrum alone, and redshift tomography improves the constraint by an additional 40%. Similar forecast for the dark energy parameters is left for future study, due to the redshift limitation of the mock convergence maps. For noisy maps, although the constraining power of the scattering coefficients is not significantly better than the combination of bispectrum and power spectrum, we argue that the scattering coefficients are still preferred, because the PDF of scattering coefficients is much more Gaussian than bispectrum coefficients.

The scattering transform yields a compact set of lower-order summary statistics that are stable, powerful, and efficient for characterizing non-Gaussian structures. Together with Cheng et al. (2020), we have shown that the scattering transform has great potential to serve as the non-Gaussian summary statistics in observational cosmology.

ACKNOWLEDGEMENTS

We thank the Columbia Lensing group (<http://columbialensing.org>) for making their suite of mock lensing maps publicly available and NSF for supporting the creation of those maps through grant AST-1210877 and XSEDE allocation AST-140041. We thank Yuan-Sen Ting for his help on image synthesis and Douglas Finkbeiner for pointing out an error in the first version of this paper. S. C. thanks Siyu Yao for her constant inspiration and encouragement.

DATA AVAILABILITY

The data underlying this article were accessed from the Columbia Lensing group (<http://columbialensing.org>). The derived data generated in this research will be shared on reasonable request to the corresponding author.

REFERENCES

- Aihara H., et al., 2018a, *PASJ*, **70**, S4
- Aihara H., et al., 2018b, *PASJ*, **70**, S8
- Ajani V., Peel A., Pettorino V., Starck J.-L., Li Z., Liu J., 2020, *Phys. Rev. D*, **102**, 103531
- Ajani V., Starck J.-L., Pettorino V., 2021, *A&A*, **645**, L11
- Allys E., Levrier F., Zhang S., Colling C., Regalado-Saint Blancard B., Boulanger F., Hennebelle P., Mallat S., 2019, *A&A*, **629**, A115
- Allys E., Marchand T., Cardoso J. F., Villaescusa-Navarro F., Ho S., Mallat S., 2020, *Phys. Rev. D*, **102**, 103506
- Andén J., Mallat S., 2014, *IEEE Transactions on Signal Processing*, **62**, 4114
- Bartelmann M., Schneider P., 2001, *Phys. Rep.*, **340**, 291
- Boyle A., Uhlemann C., Friedrich O., Barthelemy A., Codis S., Bernardeau F., Giocoli C., Baldi M., 2021, *MNRAS*,
- Bruna J., Mallat S., 2013, *IEEE Transactions on Pattern Analysis and Machine Intelligence*, **35**, 1872
- Bruna J., Mallat S., 2019, *Mathematical Statistics and Learning*, **1**, 257

- Bruna J., Mallat S., Bacry E., J.-F. M., 2015, *The Annals of Statistics*, **43**, 323
- Carron J., 2011, *ApJ*, **738**, 86
- Carron J., 2012, *Phys. Rev. Lett.*, **108**, 071301
- Carron J., 2013, *A&A*, **551**, A88
- Carron J., Neyrinck M. C., 2012, *ApJ*, **750**, 28
- Cheng S., Ting Y.-S., Ménard B., Bruna J., 2020, *MNRAS*, **499**, 5902
- Chevallier M., Polarski D., 2001, *International Journal of Modern Physics D*, **10**, 213
- Coulton W. R., Liu J., Madhavacheril M. S., Böhm V., Spergel D. N., 2019, *J. Cosmology Astropart. Phys.*, **2019**, 043
- Coulton W. R., Liu J., McCarthy I. G., Osato K., 2020, *MNRAS*, **495**, 2531
- Diaz Rivero A., Dvorkin C., 2020, *Phys. Rev. D*, **102**, 103507
- Fisher R. A., 1935, *Journal of the Royal Statistical Society*, **98**, 39
- Foreman-Mackey D., Hogg D. W., Lang D., Goodman J., 2013, *PASP*, **125**, 306
- Fu L., et al., 2014, *MNRAS*, **441**, 2725
- Hahn C., Beutler F., Sinha M., Berlind A., Ho S., Hogg D. W., 2019, *MNRAS*, **485**, 2956
- Hartlap J., Simon P., Schneider P., 2007, *A&A*, **464**, 399
- Jeffrey N., Lanusse F., Lahav O., Starck J.-L., 2020, *MNRAS*, **492**, 5023
- Jeffrey N., Alsing J., Lanusse F., 2021, *MNRAS*, **501**, 954
- Kacprzak T., et al., 2016, *MNRAS*, **463**, 3653
- Kaiser N., Squires G., 1993, *ApJ*, **404**, 441
- Kilbinger M., 2015, *Reports on Progress in Physics*, **78**, 086901
- LSST Science Collaboration et al., 2009, arXiv e-prints, p. arXiv:0912.0201
- Laureijs R., et al., 2011, arXiv e-prints, p. arXiv:1110.3193
- Li Z., Liu J., Matilla J. M. Z., Coulton W. R., 2019, *Phys. Rev. D*, **99**, 063527
- Liu J., Madhavacheril M. S., 2019, *Phys. Rev. D*, **99**, 083508
- Liu J., Petri A., Haiman Z., Hui L., Kratochvil J. M., May M., 2015a, *Phys. Rev. D*, **91**, 063507
- Liu X., et al., 2015b, *MNRAS*, **450**, 2888
- Liu J., Hill J. C., Sherwin B. D., Petri A., Böhm V., Haiman Z., 2016, *Phys. Rev. D*, **94**, 103501
- Liu J., Bird S., Zorrilla Matilla J. M., Hill J. C., Haiman Z., Madhavacheril M. S., Petri A., Spergel D. N., 2018, *J. Cosmology Astropart. Phys.*, **2018**, 049
- Mallat S., 2012, *Communications on Pure and Applied Mathematics*, **65**, 1331
- Marques G. A., Liu J., Zorrilla Matilla J. M., Haiman Z., Bernui A., Novaes C. P., 2019, *J. Cosmology Astropart. Phys.*, **2019**, 019
- Martinet N., et al., 2018, *MNRAS*, **474**, 712
- Martinet N., Harnois-Déraps J., Jullo E., Schneider P., 2021, *A&A*, **646**, A62
- Neyrinck M. C., Szapudi I., 2007, *MNRAS*, **375**, L51
- Neyrinck M. C., Szapudi I., Rimes C. D., 2006, *MNRAS*, **370**, L66
- Petri A., 2016, *Astronomy and Computing*, **17**, 73
- Petri A., Liu J., Haiman Z., May M., Hui L., Kratochvil J. M., 2015, *Phys. Rev. D*, **91**, 103511
- Pires S., et al., 2020, *A&A*, **638**, A141
- Regaldo-Saint Blancard B., Levrier F., Allys E., Bellomi E., Boulanger F., 2020, *A&A*, **642**, A217
- Rimes C. D., Hamilton A. J. S., 2005, *MNRAS*, **360**, L82
- Rimes C. D., Hamilton A. J. S., 2006, *MNRAS*, **371**, 1205
- Saydjari A. K., Portillo S. K. N., Slepian Z., Kahraman S., Burkhardt B., Finkbeiner D. P., 2020, arXiv e-prints, p. arXiv:2010.11963
- Sellentin E., Heavens A. F., 2018, *MNRAS*, **473**, 2355
- Shan H., et al., 2018, *MNRAS*, **474**, 1116
- Sifre L., Mallat S., 2013, the IEEE Conference on Computer Vision and Pattern Recognition (CVPR), pp 1233–1240
- Spergel D., et al., 2015, arXiv e-prints, p. arXiv:1503.03757
- Takada M., Jain B., 2003, *ApJ*, **583**, L49
- Tegmark M., Taylor A. N., Heavens A. F., 1997, *ApJ*, **480**, 22
- Vogeley M. S., Szalay A. S., 1996, *ApJ*, **465**, 34
- Zorrilla Matilla J. M., Haiman Z., Hsu D., Gupta A., Petri A., 2016, *Phys. Rev. D*, **94**, 083506
- van Waerbeke L., 2000, *MNRAS*, **313**, 524

APPENDIX A: BINNED BISPECTRUM

Here we describe the formulation of the binned bispectrum. The bispectrum is the products of three Fourier coefficients,

$$B(\mathbf{k}_1, \mathbf{k}_2, \mathbf{k}_3) \equiv \langle \tilde{I}(\mathbf{k}_1) \tilde{I}(\mathbf{k}_2) \tilde{I}(\mathbf{k}_3) \rangle \quad (\text{A1})$$

Because of symmetry, it is enough to consider only cases with $k_1 < k_2 < k_3$. Under statistical homogeneity, the coefficients vanish unless $\mathbf{k}_1 + \mathbf{k}_2 + \mathbf{k}_3 = 0$. To reduce the number of coefficients, one can use the binned bispectrum mono-pole, which averages the bispectrum according to the magnitude of k_1 , k_2 , and k_3

$$B_{i,j,k} = \int_{k_i}^{k_{i+1}} d\mathbf{k}_1 \int_{k_j}^{k_{j+1}} d\mathbf{k}_2 \int_{k_k}^{k_{k+1}} d\mathbf{k}_3 (2\pi)^2 \delta^{(2)}(\mathbf{k}_1 + \mathbf{k}_2 + \mathbf{k}_3) \cdot \tilde{I}(\mathbf{k}_1) \tilde{I}(\mathbf{k}_2) \tilde{I}(\mathbf{k}_3) \quad (\text{A2})$$

It is not convenient to select $\delta(\mathbf{k}_1 + \mathbf{k}_2 + \mathbf{k}_3)$ triplets within each bin. Fortunately, expanding the right-hand side of Eq. A2 in real space will simplify the integrant,

$$B_{i,j,k} = \langle (I \star f_i)(I \star f_j)(I \star f_k) \rangle, \quad (\text{A3})$$

where $f_i(\mathbf{x}) = \int_{k_i}^{k_{i+1}} e^{i\mathbf{k} \cdot \mathbf{x}} d\mathbf{k}$ is the inverse Fourier transform of the binning, an annulus in Fourier space and a wavelet-like profile in real space. This form of expression, similar to the scattering coefficients, means that the bispectrum (and other N -point functions) can also be expressed as the spatial mean of some non-linear transformation of the input field, though it has different properties from the scattering one.

APPENDIX B: COSMOLOGICAL INFERENCE FRAMEWORK

For a statistical model of observable \mathbf{x} , the Cramér–Rao inequality sets the lower limit of any unbiased estimators of model parameters obtained from the observable, therefore it can be used to quantify the uncertainty of parameter inference.

$$\text{cov}(\hat{\boldsymbol{\theta}}) \geq \mathbf{I}(\boldsymbol{\theta})^{-1}, \quad (\text{B1})$$

where $\mathbf{I}(\boldsymbol{\theta})$ is the Fisher information matrix, whose elements are defined as

$$I_{m,n}(\boldsymbol{\theta}) \equiv - \left\langle \frac{\partial \ln p(\mathbf{x}|\boldsymbol{\theta})}{\partial \theta_m} \frac{\partial \ln p(\mathbf{x}|\boldsymbol{\theta})}{\partial \theta_n} \right\rangle. \quad (\text{B2})$$

In our case, $\boldsymbol{\theta}$ is the cosmological parameters, and \mathbf{x} is the vector of summary statistics such as the scattering coefficients. The PDF is assumed to be Gaussian,

$$p(\mathbf{x}|\boldsymbol{\theta}) \propto \frac{1}{\sqrt{|\mathbf{C}|}} \exp\left[-\frac{1}{2}(\mathbf{x} - \boldsymbol{\mu})^T \mathbf{C}^{-1}(\mathbf{x} - \boldsymbol{\mu})\right], \quad (\text{B3})$$

where $\mathbf{C}(\boldsymbol{\theta})$ is the covariance matrix of summary statistics. We further assume $\mathbf{C}(\boldsymbol{\theta})$ is cosmology independent. Thus, the Fisher matrix becomes

$$I_{m,n} = \frac{\partial \boldsymbol{\mu}^T}{\partial \theta_m} \mathbf{C}^{-1} \frac{\partial \boldsymbol{\mu}}{\partial \theta_n}. \quad (\text{B4})$$

We use linear or second-order polynomials to fit the cosmological dependence of the mean vector $\boldsymbol{\mu}(\boldsymbol{\theta})$, and use the sample covariance matrix $\widehat{\mathbf{C}}$ estimated from simulations at fiducial cosmologies ($\Omega_m = 0.26$, $w_0 = -1$, $w_a = 0$ for the dark energy dataset and $\Omega_m = 0.3$, $M_\nu = 0$, $A_s = 2.1 \times 10^{-9}$ for the MassiveNuS dataset) to estimate the inverse of covariance matrix (Hartlap et al. 2007):

$$\widehat{\mathbf{C}}^{-1} = \frac{N - D - 2}{N - 1} \widehat{\mathbf{C}}^{-1}, \quad (\text{B5})$$

where $\widehat{\mathbf{C}}^{-1}$ is an unbiased estimator, N is the number of independent sample used for the estimation (1,000 for the dark energy dataset and 10,000 for the MassiveNuS dataset), D is the number of summary statistics used, which is 36, 30, and 125 per redshift bin, for scattering coefficients, binned power spectrum, and binned bispectrum, respectively. The covariance matrix \mathbf{C} of summary statistics is measured from $3.5 \times 3.5 \text{ deg}^2$ maps. To make a forecast for Rubin-like surveys with $20,000 \text{ deg}^2$, we simply scale the covariance matrix by a factor of $3.5 \times 3.5 / 20,000$, which is equivalent to assuming that each $3.5 \times 3.5 \text{ deg}^2$ patches are independent. Though not exactly correct, this is still a common approximation to get a quick forecast without running many full-sky simulations (e.g., Li et al. 2019; Liu & Madhavacheril 2019; Coulton et al. 2019).

The Bayesian posterior is another way to quantify the uncertainty of model parameter inference. Given the likelihood $p(\mathbf{x}|\boldsymbol{\theta})$, the posterior probability distribution of model parameter is

$$p(\boldsymbol{\theta}|\mathbf{x}) \propto p(\mathbf{x}|\boldsymbol{\theta})p(\boldsymbol{\theta}), \quad (\text{B6})$$

where $p(\boldsymbol{\theta})$ is the prior distribution of $\boldsymbol{\theta}$. For the noisy cases with MassiveNuS, we use a flat prior in $\Omega_m \in [0.28, 0.32]$, $M_\nu \in [0.06, 0.6] \text{ eV}$, and $A_s \in [1.8, 2.7] \times 10^{-9}$ to avoid extrapolation. The posterior is then sampled using `emcee` (Foreman-Mackey et al. 2013), a Markov Chain Monte Carlo (MCMC) sampler. We used 32 walkers, ran 1,000 steps to burn-in and then 10,000 steps to sample the posterior. Sampling convergence was checked within and among chains. For all combinations of summary statistics used in Figure 6, the auto correlations of the chain are measured to be within $\pm 2 \%$ when the distance is longer than 100 steps.

This paper has been typeset from a $\text{\TeX}/\text{\LaTeX}$ file prepared by the author.